NDT&E International 156 (2025) 103489

Contents lists available at ScienceDirect

NDT and E International

journal homepage: www.elsevier.com/locate/ndteint

Research Paper

# Enabling near-array ultrasonic imaging with an apex-shifted Radon transform

Augustine E. Loshelder, Jiaze He *, John D. Day, Md. Aktharuzzaman, Weihua Su *

*Department of Aerospace Engineering and Mechanics, The University of Alabama, Tuscaloosa, 35487-0280, AL, USA*

ARTICLE INFO

*Keywords:*
Apex-shifted Radon transform
Total focusing method
Ultrasonic imaging
Nondestructive evaluation and testing

ABSTRACT

This paper presents an ultrasonic signal processing technique based on the apex-shifted Radon transform (ASRT) to mitigate near-array artifacts as a more selective filtering alternative to conventional time-gating strategies for the total focusing method (TFM). The ASRT-based image processing algorithm described here is used to selectively mute the direct P-waves and surface waves (collectively referred to as direct arrivals) by their geometry in the time–space domain of full matrix capture data before performing TFM, which are the sources of near-array artifacts. First, a mathematical formulation and intuitive explanation of the ASRT is provided. Then, the algorithm's ability to improve near-array image clarity is demonstrated on a synthetic model of a steel region with two small inclusions near the array. Here, a significant reduction of the "dead-zone" artifacts is observed. Then, the algorithm's performance is shown to be comparable when applied to experimental data obtained from an Inconel block with holes. From this investigation, the ASRT is concluded to be an effective tool for enabling ultrasonic imaging within a wavelength of the array.

## 1. Introduction

Ultrasonic inspection is a mainstay of nondestructive evaluation (NDE) and material characterization due to its accessibility and flexibility. Accurate ultrasonic inspections are achievable with relatively inexpensive hardware and offer a high degree of customization to the sensor array. These inspections also benefit from being fast and can be completed in real-time or in a matter of seconds. Because of these benefits, ultrasound is highly convenient for laboratory, in-situ, and manufacturing scenarios [1–7].

In the field of nondestructive evaluation, ultrasonics are widely used for defect characterization [8,9]. When ultrasonic waves interact with defects such as cracks, porosities, and impurities, they cause a detectable signature in the received signals [10]. The damage detection capabilities of ultrasound are well-documented for rail components [11], welded parts [12], composite parts such as aircraft components [13], and heterogeneous media like polycrystalline solids [14].

Raw ultrasonic measurements may be processed in various ways to glean the most relevant information from the scanned specimen. For a topographical approach, these measurements will be input into an ultrasonic imaging algorithm to produce a map of the scanning region characterized by the differences in its physical properties. Defects, grain boundaries, and the constituents of a composite part have different physical properties from the surrounding media, which causes changes to the wave propagation and allows ultrasonic imaging algorithms to resolve these regions visually. Several ultrasonic imaging algorithms are available, including the total focusing method (TFM), phase coherence imaging (PCI), and full-waveform inversion (FWI). TFM uses a delay-and-sum calculation to quickly resolve a reflectivity map in a specimen [15,16]. PCI is a similar method to TFM, yet it relies on the phase dependence of scattered waves to image [17]. FWI is a significantly more expensive process adapted from geophysics, which employs wave propagation simulation and gradient calculations to iteratively converge to an accurate material property map [18]. From these methods, TFM, in particular, has become a popular research topic in NDE due to its simple implementation, relatively fast processing time, and accuracy.

One major limitation in ultrasonic imaging, and for TFM in particular, is the "dead-zone effect" [19], which imposes a minimum distance from the scanning array that an image can be clearly resolved. This effect is caused by the high-amplitude waves propagating directly out from the source *(direct waves)* and along the surface *(surface waves)* that occupy some portion of the early received signals, which can obscure wave packets from defects and other areas of interest near the array. The relative dominance of these "direct arrivals" in the time-domain ultrasonic signal is primarily a function of the material wavespeed, excitation time, and excitation frequency, whose presence directly influences the size of the dead zone. Without compensating

* Corresponding authors.
*E-mail addresses:* jiazehe@gmail.com (J. He), suw@eng.ua.edu (W. Su).

https://doi.org/10.1016/j.ndteint.2025.103489
Received 21 April 2025; Received in revised form 16 July 2025; Accepted 16 July 2025
Available online 26 July 2025

for the dead-zone effect, ultrasonic imaging algorithms will attempt to process the direct arrivals, which can lead to strong artifacts in the case of TFM.

There are various approaches to overcome the dead-zone effect [20,21]. Repositioning the scanning array allows the dead zone to be moved outside the region of interest. However, it requires multiple acquisitions. In addition, the specimen must be large and accessible enough to be scanned from multiple points. Wedge transducers, in particular, have been shown to be effective in reducing the dead-zone depth [21]. Time-gating simply images the portion of the signals after the direct arrivals, which negates any artifacts but prevents the near-array region from being imaged at all [22]. Thresholding is a similar strategy that can overcome the amplitude disparity between the direct arrivals and scattered signals by limiting the signal amplitudes to a certain maximum value. However, this strategy is ineffective in cases where the direct arrivals overlap with the scattered wave groups. More selective masking is possible through strategies such as the normal moveout correction (NMO), which allows the direct arrivals to be targeted surgically. However, by deleting the direct arrival waves, any overlapping scattered waves will also be partially destroyed [23]. Ha et al. [24] introduced the technique of using an autoencoding neural network to detect defects within the dead zone. However, imaging such defects is not the primary focus of such a technique.

This paper proposes a selective approach to muting these direct arrival wave groups via the Apex-shifted Radon transform (ASRT) [25,26], which can mitigate dead-zone artifacts and enable clearer near-array imaging. The ASRT is a generalized Radon transform, a signal processing technique introduced in 1917 [27] and popularized in geophysics, where it is employed for denoising [28] and multiple attenuation [26,29] tasks. Denoising is a familiar term in the domain of NDE, referring to the task of enhancing the signal-to-noise ratio of the receiver signals. Multiple attenuation refers to tasks that mute signals of multiply-reflected wave packets to emphasize the primary reflections. In both cases, the ASRT is used to process seismic signals by either isolating or muting targeted portions of the data to emphasize useful information and de-emphasize spurious readings and clutter. Similarly, for SHM and NDE ultrasonics, it is applied to the time–space ultrasonic signals during preprocessing. This work is a continuation of the work in applying ASRT to an ultrasonics setting [30]. The ASRT transforms the time–space domain wave packets into a new domain parameterized by their geometry via path integration. Then, in the Radon domain, isolating or deleting specific elements of the signals becomes much easier with minimal perturbation to the nearby data. In the previous paper, the ASRT is used as a wave packet extraction algorithm primarily for denoising tasks. In this investigation, however, the ASRT is used for the inverse task as a wave packet deletion technique to mute the direct arrivals received by an ultrasonic transducer. Additionally, whereas the original work maintains a focus on ultrasonic signals and a structural health monitoring discipline, this work is concerned with the effects of the ASRT on TFM images. This manuscript will first detail the theory and working principle of the ASRT-based dead-zone compensation technique, along with an overview of ultrasonic array scanning and TFM. Next, the technique is demonstrated on a numerical model of a steel region with two near-array inclusions that are occluded by near-array artifacts as a feasibility study. The technique is subsequently applied to real data acquired from an additively manufactured Inconel specimen for experimental validation. Some discussion is included about the other uses of the ASRT in ultrasonic testing, and the conclusions and potential future work are summarized.

## 2. Theory and working principle

### 2.1. The total focusing method and near-array artifacts

Ultrasonic array data is acquired via source–receiver pairs, where the signal source is an element that excites ultrasonic waves in the medium, and the receiver is the element that measures received amplitudes. The receiver records a time-domain signal, which is a one-dimensional measurement of a wave signal sampled over a finite time. It is common for some or all of these elements to serve as both sensors and receivers. These elements can then be arranged into an *array* of various shapes, including linear and ring-shaped, which allows for better coverage of the specimen [31].

The acquired time-domain receiver data are stored in a three-dimensional digital object, organized by receiver number and source event. This is a common ultrasound data storage strategy referred to as full matrix capture (FMC) [32]. FMC provides a convenient method of analyzing the received ultrasonic signals, as slices of the 3-D object can be viewed independently to understand the response from a specific source excitation or at a specific receiver across each source. When all FMC data is interpreted with a delay-and-sum imaging algorithm, the result is the total focusing method (TFM). FMC and TFM are very popular data acquisition strategies and imaging methods in ultrasonic inspection. One common issue in TFM is the presence of a near-array artifact caused by surface waves and direct waves (referred to together for bulk wave imaging as "direct arrivals") as shown in Fig. 1. This effect can be aggravated by lengthy or low-frequency excitation and low material wavespeeds, all of which increase the relative proportion of signal occupied by the direct arrivals.

### 2.2. Apex-shifted Radon transform

The proposed filtering technique relies on the apex-shifted Radon transform (ASRT), which is a family of line-integral transforms that collect the energy of a scalar field along a specified geometry. This geometry is often a polynomial or conic section, making it ideal for collecting wave packets from time–space ($t$ - $x$) domain ultrasonic signals since linear shapes (such as direct arrivals from a linear array) and hyperbolic shapes (such as the scatter from a point-like defect as received by a linear array) are common. The ASRT generally parametrizes these geometries by their curvature and their horizontal and vertical axis offset values. In the case of this paper, a linear ASRT is used in the $t$ - $x$ domain ultrasonic signals, so that the "curvature" is simply the inverse of the wavespeed, the horizontal offset is the receiver position, and the vertical offset is the time coordinate. The Radon image of a well-captured shape will appear at the coordinate of the geometry's *apex*, which is the central axis of symmetry/antisymmetry. For instance, a line's apex is its $y$-intercept, and a hyperbola's apex is its vertex.

The general discrete polynomial forward ASRT [25] is

$$m(\tau, q_k, y_i) = \sum_{j=0}^{n_x-1} d(t = \tau + q_k(y_i - y_0)^n, x_j), \quad k = 0, \dots, n_q - 1, \quad i = 0, \dots, n_y - 1, \tag{1}$$

where $m$ represents the model Radon domain, and $d$ denotes the original data domain. The Radon domain is a 3-dimensional region parameterized by $\tau$, the time delay, $q$, the Radon coefficient that defines curvature, and $y$, the apex-offset value. For the linear Radon transform employed in this paper, parameter $q$ is defined as $time/distance$, which is the *slowness* quantity and corresponds to the inverse wavespeed of a wave group. The apex offset parameter $y$ is used to perform the ASRT with respect to each $y_i$, which corresponds to a specific apex location as an offset from $y_0$, the reference $y$ value generally assigned as the left edge of the $t$ - $x$ domain. Then, $n_x$ is the number of receivers, $n_y$ is the number of apex locations, and $n_q$ is the number of curvature bands used in the transform. In addition to the number of selected apex locations $n_y$, the curvature is sampled at a density according to the total width of the curvature band $q$ divided by the number of samples $n_q$. The chosen values of $n_q$ and $n_y$ heavily impact the resolution and computational expense required to compute the Radon transform, which is inversely related to the resolution of the transform.

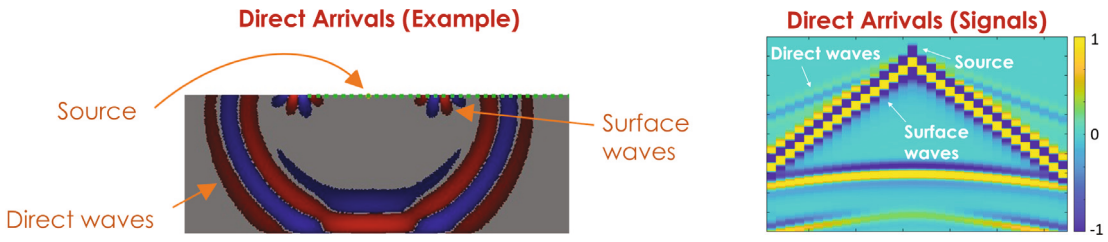


(a) (b)

**Fig. 1.** An illustration of the concept of "direct arrivals", which are the direct wave and surface wave groups. Direct waves propagate directly radially outward from the source location and are generally high in amplitude, and surface waves propagate along the surface when the source is located there, and are often the highest amplitude wave group in $t$ - $x$ data. In part (a), a wavefield snapshot containing these two wavegroups is included, and in part (b) the $t$ - $x$ domain representation of these waves is shown.

For this application, the ASRT is used to target the ultrasonic direct arrivals, which emanate from the excitation source. As such, the apex location $y_i$ will generally correspond to the spatial position of the source or sources, and in the case of a single-source excitation, only one $y_i$ needs to be considered, making the Radon domain effectively 2-D. Similarly, $t$ and $x$ correspond to the time and space coordinates, and $x$ is generally discretized by each receiver position (i.e., the ultrasonic array's pitch).

An inverse ASRT exists to restore the Radon domain data to its original $t$ - $x$ domain. The discrete inverse ASRT is defined as

$$d(t, x_j) = \sum_{k=0}^{n_q-1} \sum_{i=0}^{n_y-1} m(\tau, q_k, y_i), j = 0, \ldots, n_x - 1. \tag{2}$$

To facilitate implementing the ASRT digitally, the following steps are taken to represent the ASRT as a matrix operation: By taking the temporal Fourier transform of Eq. (2), the inverse ASRT can be represented in the frequency domain as

$$D(\omega, x_j) = \sum_{k=0}^{n_q-1} \sum_{i=0}^{n_y-1} M(\omega, q_k, y_i) e^{-i\omega q_k (x_j - y_i)^n}, \tag{3}$$

where $D$ and $M$ are the Fourier transformed data and model domains respectively, now indexed by frequency $\omega$ instead of time coordinates $t$ and $\tau$.

Eq. (3) can then be written in terms of matrix operations, i.e.,

$$\mathbf{D} = \mathbf{LM}. \tag{4}$$

where $\mathbf{D}$ and $\mathbf{M}$ are the matrix forms of the frequency domain data and model domains. $\mathbf{L}$ is the apex-shifted Radon operator, which takes the form of $n_y$ many $\mathbf{L}_i$ matrices of size $n_x \times n_q$ concatenated, each representing apex-offset value $y_i$. $\mathbf{L}$ is defined by

$$\begin{bmatrix} \mathbf{L}_1 & \mathbf{L}_2 & \cdots & \mathbf{L}_{n_y} \end{bmatrix} \tag{5}$$

where each submatrix $\mathbf{L}_i$ is defined as

$$\mathbf{L}_i = \begin{bmatrix} e^{-i\omega q_0 (x_0 - y_i)^n} & e^{-i\omega q_1 (x_0 - y_i)^n} & \cdots & e^{-i\omega q_{n_q-1} (x_0 - y_i)^n} \\ e^{-i\omega q_0 (x_1 - y_i)^n} & e^{-i\omega q_1 (x_1 - y_i)^n} & \cdots & e^{-i\omega q_{n_q-1} (x_1 - y_i)^n} \\ \vdots & \vdots & \ddots & \vdots \\ e^{-i\omega q_0 (x_{n_x-1} - y_i)^n} & e^{-i\omega q_1 (x_{n_x-1} - y_i)^n} & \cdots & e^{-i\omega q_{n_q-1} (x_{n_x-1} - y_i)^n} \end{bmatrix}. \tag{6}$$

Fig. 2 provides an intuitive graphical depiction of the discretized ASRT as shown with a general symmetric curve shape. In practice, there are many shapes along which this summation can be calculated, including linear, parabolic, and hyperbolic. Each of the three will best capture wave packets that appear in the time–space domain as similar to the selected shape. The energy along the three parameters of the Radon domain is collected by a summation represented by the dotted green lines. A summation is performed with respect to each possible curvature or slope, time coordinate, and apex location in the domain. Here, the apex refers to the axis of symmetry or antisymmetry on the selected curve shape and is the point of focus for the ASRT. The energy collected by the summation is then transformed into the 3-D Radon domain, where the geometry of interest is now collected in discrete point-like regions indexed by the apex time, apex location, and curvature parameters.

**Table 1**
SPECFEM2D steel two-inclusion simulation parameters.

| Parameter | Symbol | Value | Unit |
|---|---|---|---|
| Time step size | $dt$ | 25 | ns |
| Vertical grid size | $dz$ | 1.833 | mm |
| Horizontal grid size | $dx$ | 1.833 | mm |
| # of vertical spectral elements | $n_z$ | 60 | – |
| # of horizontal spectral elements | $n_x$ | 60 | – |
| # of sources | $n_S$ | 32 | – |
| # of receivers | $n_R$ | 32 | – |
| Array pitch | – | 2.9 | mm |
| Array width | – | 89.9 | mm |
| Array central frequency | $f$ | 0.5 | MHz |

### 2.3. Error quantification

The effectiveness of the ASRT for the direct arrival mute task can be quantified by the ratio of the power of the desired defect-scattered signals, $P_S$, to the undesirable direct arrival signals, $P_D$. The increase of this power ratio can then be used to indicate the degree of improvement from the ASRT-based processing. This is effectively a signal-to-noise ratio (SNR) calculation, a common quantity that can be expressed in terms of a power ratio.

The power ratio $\frac{P_S}{P_D}$ can be expressed in decibels (dB) as

$$\frac{P_S}{P_D} = 20 \cdot \log_{10} \left( \frac{A_S}{A_D} \right). \tag{7}$$

Here, $A_S$ and $A_D$ are the root mean square (RMS) amplitudes of the signal's scattered and direct portions respectively.

## 3. Mitigating near-array artifacts in numerically simulated steel

To demonstrate the use of the ASRT to mute direct arrivals for enabling near-array imaging, a synthetic proof-of-concept is constructed using the spectral element wave propagation solver SPECFEM2D and a python framework, SeisFlows [33–36]. A 110 mm × 110 mm square steel region is created with two inclusions of an arbitrary wavespeed, as seen in Fig. 3(a). The simulation is initialized with an array of 32 elements with a pitch of 2.9 mm centered over the domain. The domain is modeled using 60 × 60 spectral elements, and the simulation uses a 25 ns time step size. The relevant simulation parameters are collected in Table 1. The simulation employs a perfectly matched layer (PML) absorbing boundary, which negates any boundary reflection behavior. Compared with holes, inclusions like the ones present in this model induce weaker scattered waves that are likely to be buried by the direct arrival waves. These inclusions are within 3 and 7 wavelengths of the

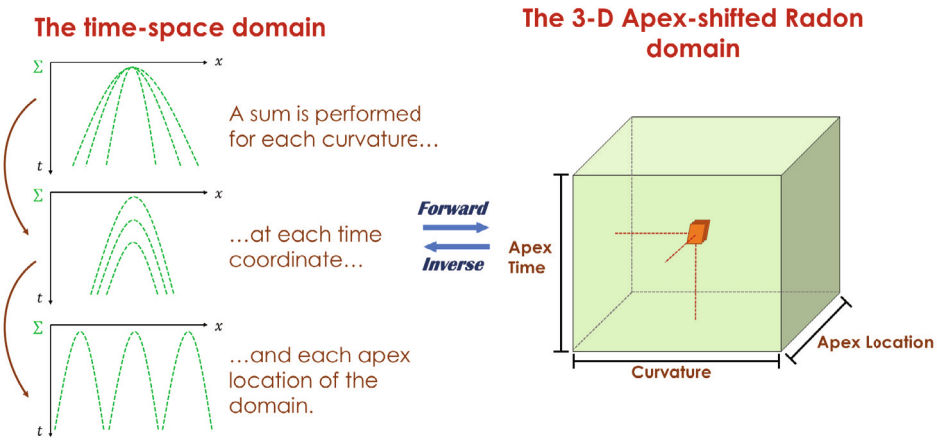


**Fig. 2.** An intuitive diagram of the apex-shifted Radon transform process. From the $t$ - $x$ domain signals, a summation is performed with respect to the three Radon domain parameters curvature $q$, apex time $\tau$, and apex spatial location $y$. This results in a 3-D Radon domain that can be restored to the original domain via the inverse ASRT.

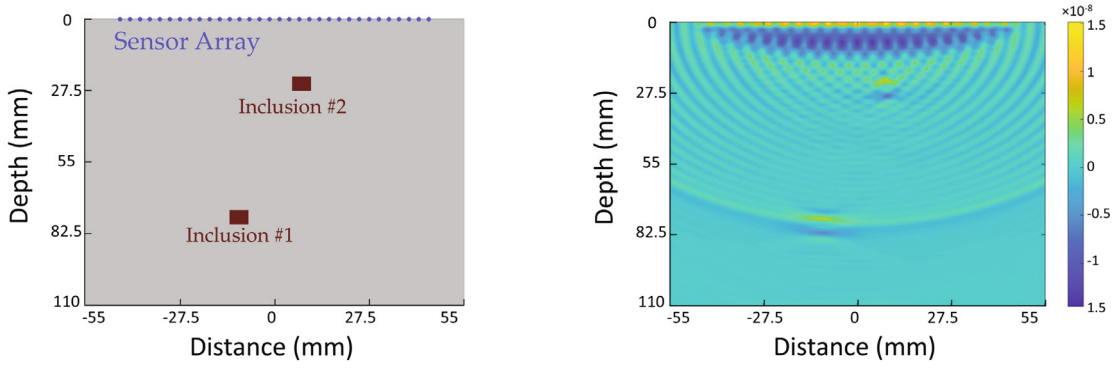


**Fig. 3.** A 2-D numerically simulated steel specimen with two inclusions. Part (a) is a schematic of the steel region containing two inclusions. Part (b) is the TFM image of the raw signals obtained from the steel region.

array, respectively, making the near inclusion especially challenging to image.

From Fig. 3(b), it can be seen that the presence of these obscuring near-array artifacts worsens the visibility of both artifacts. The proposed ASRT-based processing tool is then used to mute the undesirable artifact in a process outlined in Fig. 4.

First, the raw data is thresholded by limiting the received signal magnitudes to a value slightly greater than the scattered wave intensity. This limits the disparity of intensity between the direct arrivals and scattered waves without altering the intensity of the scattered waves (Fig. 4(b)), which will result in a more balanced distribution of values in the Radon domain. To understand the utility of thresholding, Fig. 6 compares the results of performing the Radon transform on non-thresholded and thresholded input signals. In the non-thresholded case, the Radon domain representation of the source signature is significantly overshadowed by its highest amplitude components, and filtering tasks may struggle to identify the entire source signature. In the thresholded case, the Radon signature of the source is significantly longer (along the vertical time axis) and is more easily processed. As previously mentioned, performing TFM on the unfiltered signals produces a highly artifacted result Fig. 4(c). Instead, in Fig. 4(d), the Radon transform is applied to the thresholded data, converting the 3-D FMC object into a 4-D tensor with dimensions of time, slowness, the number of events, and the number of focusing axes in the Radon domain.

Assuming a point-source excitation and a linear array (a common ultrasonic scanning setup) allows for simplification. When only one source is activated, the direct arrivals will always emanate from that source location, so the dimension of focusing axes should be limited to only the source location. In the case of a one-dimensional linear array, the linear Radon transform is sufficient because the direct arrivals are themselves expected to be linear.

With these assumptions in place, the filtering task in the Radon domain becomes trivial. Since the information in the Radon domain is characterized by its vertical intercept value, the filtering task can be limited to the curvature band at the early-time portion of the Radon domain where the direct arrivals converge. This has the added benefit of limiting the number of apex locations, $n_y$, to one, significantly reducing the computational expense of the process. In this case and the following cases, the Radon curvature is sampled at 401 discrete bands, such that $n_q = 401$. Based on the authors' experience, these parameters are an effective compromise between computational expense and resolution. By selecting the region around the intercept at the source coordinate as in Fig. 4(d), both linear "arms" of the direct arrival will focus in the Radon domain at symmetric locations. The entire band of curvature can be deleted rather than surgically muting the target regions. Along the time axis, the duration to mute is decided by visual inspection. From Fig. 4(b), the direct self-excitation of Source 15 is concluded by 5 μs, as do the Radon domain signatures corresponding to the direct arrivals in Fig. 4(d). Therefore, the first 5 μs of the Radon domain are muted for the entire curvature spectrum, meaning that all linear wave packets intersecting this region are significantly attenuated after filtering and reconstruction.

After returning the filtered receiver data from the Radon domain to the time–space domain, the signature of the direct arrivals is drastically

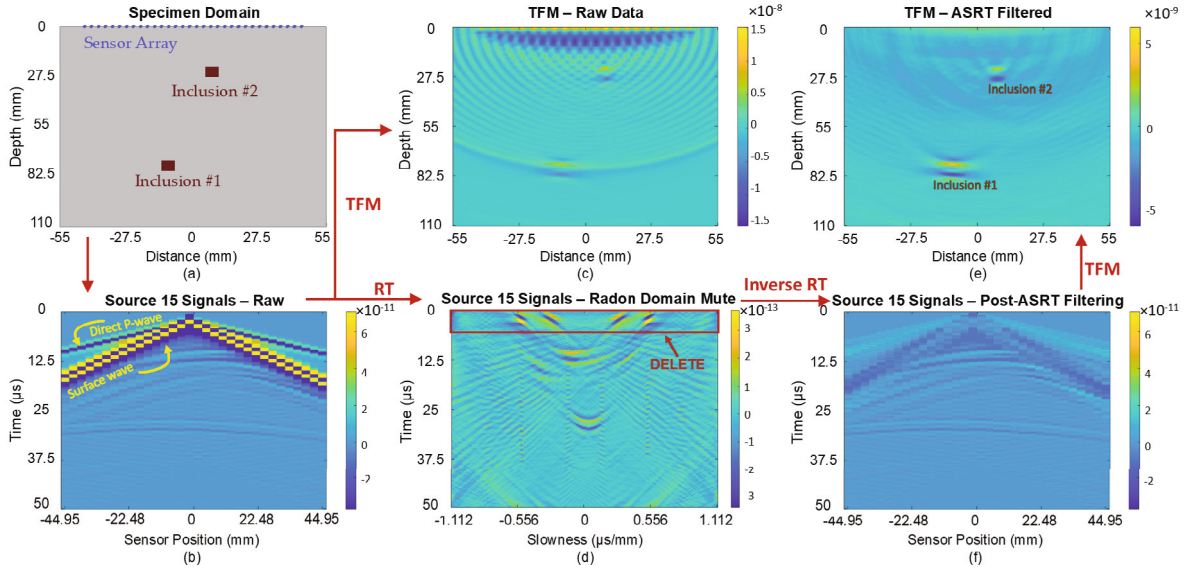


**Fig. 4.** The ASRT-based near-array artifact mute technique in flowchart form as demonstrated on a numerical simulation of a steel region with two inclusions. In part (a), the numerically simulated domain is shown. In part (b), the raw signals obtained from this region are displayed, which can be directly imaged with TFM to produce a heavily artifacted image as in part (c). Instead, by performing the ASRT in (d), the direct arrivals causing this artifact can be filtered out by eliminating the early-time band of the Radon domain as shown, producing a clearer image (e) from signals (f).

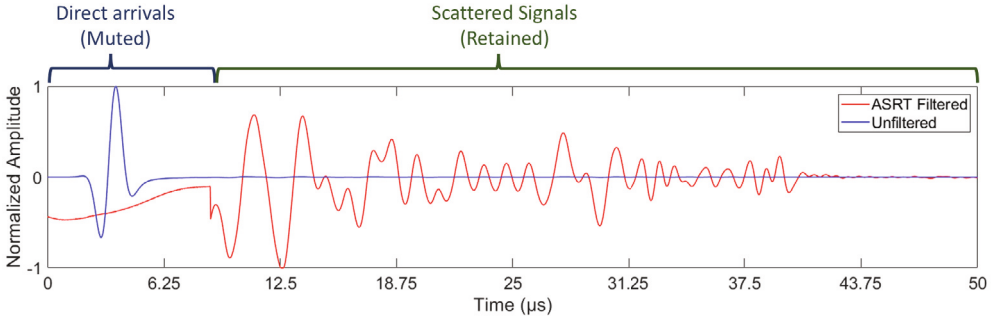


**Fig. 5.** Comparison of the unfiltered (blue line) and ASRT-filtered (red line) received signals for the source 15-receiver 15 pair of the numerical steel data. The signals are normalized to their respective maximum values for comparison. For the unfiltered case, only the source excitation signal is visible, and the response of the domain is nearly invisible due to its comparatively small magnitude. When the threshold and ASRT are used, the source signal is muted and the response becomes clearly visible with minimal artifacts from the ASRT. This is consistent with the calculated 38.723 dB improvement to the power ratio. In this numerical case, the ASRT is found to eliminate the shape of the source signature almost entirely.

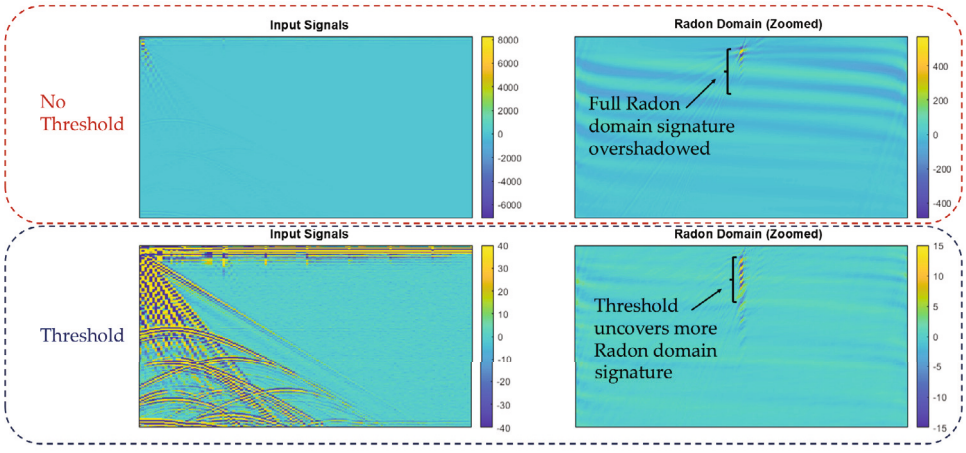


**Fig. 6.** The results of performing a Radon transform on a non-thresholded and thresholded set of signals. In the non-thresholded case, the data amplitude is left unmodified, and has a maximum magnitude of 8000. When the Radon transform is performed, the signature of the target region is overshadowed by a highly intense region at its top. By thresholding to an amplitude of |40|, the Radon domain signature is significantly better defined, and editing tasks can be performed with greater precision.

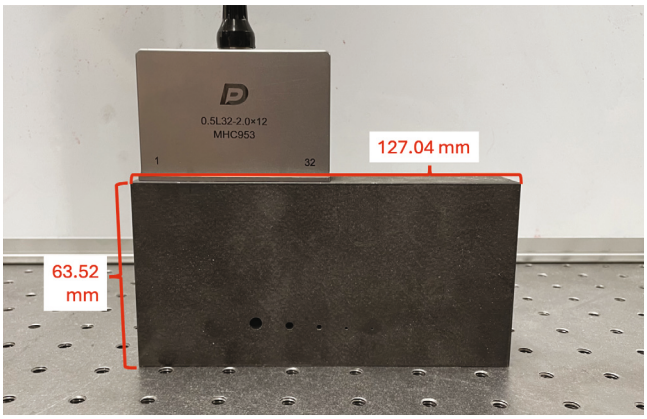


**Fig. 7.** The Inconel specimen data acquisition setup with a linear array transducer mounted on the top surface, centered over the largest hole. Due to a limited aperture and frequency, the objective is to image the three largest/closest holes. The holes are of decreasing size and are aligned by their bottom edge. This test is repeated twice, once with the specimen in this "far-hole" configuration and also flipped over its horizontal in the "close-hole" configuration.

lowered, as seen in Fig. 4(f). In this case, the combined thresholding and ASRT processes reduce the direct arrivals to 1/350 of their original amplitude. Some remaining energy from the direct arrivals is still seen in Fig. 4(f), the significance of which is related to the choice of Radon domain muting strategy. For this investigation, a rectangular region is muted (as in Fig. 4(d)) for ease of implementation, but more advanced selection techniques exist in literature [29].

Finally, TFM can be performed on the ASRT-filtered signals, allowing for comparison between the raw and masked signals (Fig. 4(e)). The power ratio metric described in Eq. (7) can be used to compare the improvement of the ASRT-based mute technique using the source 15 receiver 15 pair. For the presented results, the unfiltered signals have a power ratio of $-45.008$ dB, while the filtered signals have a power ratio of $-6.285$ dB. This gives an improvement of 38.723 dB. This power ratio increase is clearly seen in Fig. 5, which compares the time-domain representation of the centrally located source 15-receiver 15 pair signals for the unfiltered and filtered cases. In the unfiltered raw signal, the only clearly visible response is the direct arrivals. When the ASRT-based filtering is used, the increased relative amplitude of the scattered signals compared to the source signature accounts for the improved contrast of the defects in the TFM image. Due to the high resolution and the lack of reflections, noise, and other outside influences, the technique is shown to almost eliminate the direct arrivals for this source and receiver pair.

## 4. Near-array imaging in experimental data

To validate the ASRT-based near-array artifact mute, the process as presented above is applied to experimental measurements from an additively manufactured Inconel specimen with an array of holes spanning the width, pictured in Fig. 7.

The specimen is scanned using a 0.5 MHz linear array transducer with 32 elements and a pitch of 2 mm centered over the largest hole from both the far- and near-sides relative to the holes. The far-side scan setup is depicted in Fig. 8(a), and the near-side case in Fig. 10(a). In both cases, each of the 32 elements excites a five-peak signal in the Inconel specimen one by one, and all elements act as receivers. Received amplitudes are measured at a sampling frequency of 10 MHz for $1 \times 10^{-4}$ s. The signals from this scan are stored in a size $1000 \times 32 \times 32$ FMC object, with the 15th source slice given as a visual example in Fig. 8(b).

The Inconel medium used here was previously determined to have a wavespeed of 5700 m/s, so for the 0.5 MHz excitation, the holes in the far-side case will be within five wavelengths from the array and the close-side case will be approximately one wavelength away. Performing TFM on the raw data obtained by these scans as in Fig. 8(c) and Fig. 10(c), the near-array artifacts are found to have by far the highest signature in the region, covering nearly half of the domain and confirming this prediction.

First, the far-hole case is considered in Fig. 8. To mitigate the near-array artifacts, the ASRT mute process is applied. As in the numerical example, the domain is first thresholded. Next, the forward Linear ASRT is calculated for each source as seen in Fig. 8(d), where the direct arrivals are collected along the top band in two symmetric regions of high energy. This band is deleted, heavily reducing the signature of linear regions of all slopes intercepting the source coordinate for the first 13.97 50 μs (220 samples), which is a filtering condition designed to eliminate the direct arrivals specifically from the received signals. After performing an inverse ASRT, the TFM image of the filtered data can be obtained as in Fig. 8(e), and the filtered signals that produced this TFM image can be seen in Fig. 8(f) with the direct arrivals heavily attenuated. In the filtered case, this artifact is reduced by about 90%. In this case, since the holes are about five wavelengths from the array and the excitation signal is five-peaked, there is a significant overlap between the direct arrivals and the hole-scattered waves. Hence, the artifact reduction is significant and nontrivial to produce. For this case, the unfiltered signals give a power ratio of $-42.438$ dB, and the filtered signals give a power ratio of $-4.240$ dB, indicating a 38.198 dB improvement. As in the numerical case, the source 15-receiver 15 signal shows the relative amplitude improvement of the scattered signals in Fig. 9. For the far-hole case, the source signature remains largely unchanged, except for minor shape distortion. However, the relative amplitude of the scattered signals is significantly higher in the filtered case. There are some spurious artifacts in the early portion of the scattered signals, where the ASRT has not perfectly captured the undesirable signal components. However, the overall shape remains unchanged, and the filtered case functions well for TFM imaging. Next, in the considerably more difficult close-hole case seen in Fig. 10, the same process is repeated, starting with the raw signals in Fig. 10(b). In this case, the holes are about one wavelength from the array, meaning there is a very significant overlap between the direct arrivals and the target hole-scattered waves. The direct arrival waves filtered in the Radon domain (Fig. 10(d)), resulting in clean signals (Fig. 10(f)). Compared to the raw TFM image in Fig. 10(c), the filtered TFM in Fig. 10(e) has significantly better image quality, and the holes in the specimen have become identifiable. This is a significant result, as the artifacts induced by the near-array effects would otherwise pollute the image too much to visually discern the holes. In the far hole case, the unfiltered signals have a power ratio of $-41.791$ dB, and the filtered signals give a $-12.575$ dB ratio, which shows a 29.217 dB increase. To show this power ratio increase, Fig. 11 again compares the unfiltered and filtered signals for the source and receiver pair at element 15. In this more difficult case, some additional shape distortion is present, seemingly due to interactions between the direct arrivals and scattered signals, which create more difficult shapes for the ASRT to capture. Since the frequency content is mainly undamaged, however, the TFM image is still found to accurately detect the presence of defects. The power ratio improvements are tabulated in Table 2 for comparison between cases.

From the cases presented here, the ASRT near-array artifact mute technique is effective on real data with a similar performance to the numerical example. In the far-hole example, the potentially large presence of the near-array artifact is emphasized, with the pollution of nearly the entire specimen domain obscuring the holes near the bottom edge. In the close-hole case, the algorithm's capability to uncover the holes at approximately one wavelength distance from the array is demonstrated.

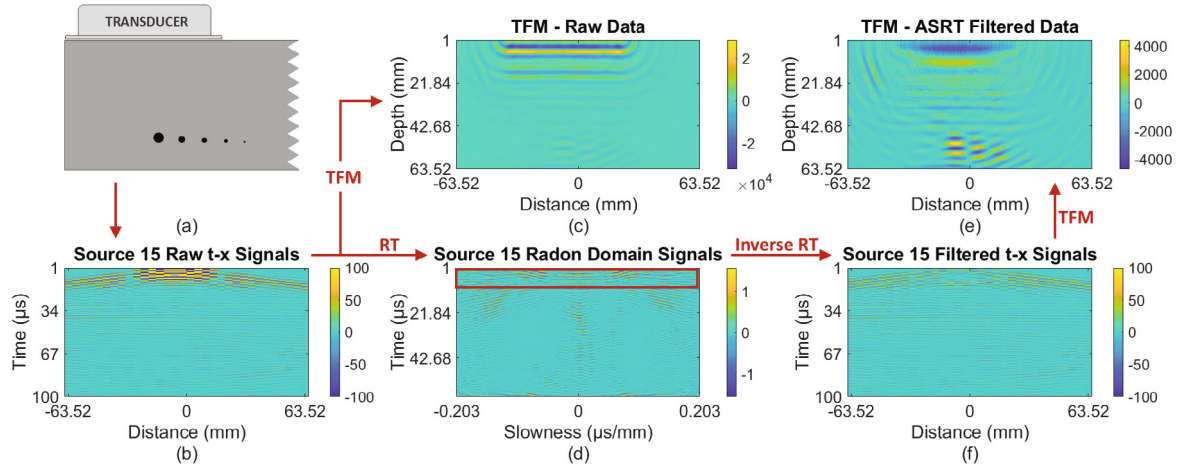


**Fig. 8.** The ASRT near-array artifact mute process as applied to real data from an Inconel block with holes. In part (a), the Inconel specimen is represented, from which specimen the raw signals in part (b) are obtained. Directly imaging with TFM using the raw signals provides an unclear image as in part (c) which must be aggressively thresholded to visually identify the signature of the holes. Instead, the ASRT is performed as in part (d), where the early-time curvature band of the Radon domain is muted at each source location in a slice-by-slice fashion of the total FMC object. By imaging the filtered signals, the artifact presence is reduced by a factor of 10 as seen from part (e), and an example of the filtered signals used to produce this image from the source 15 excitation are given in part (f).

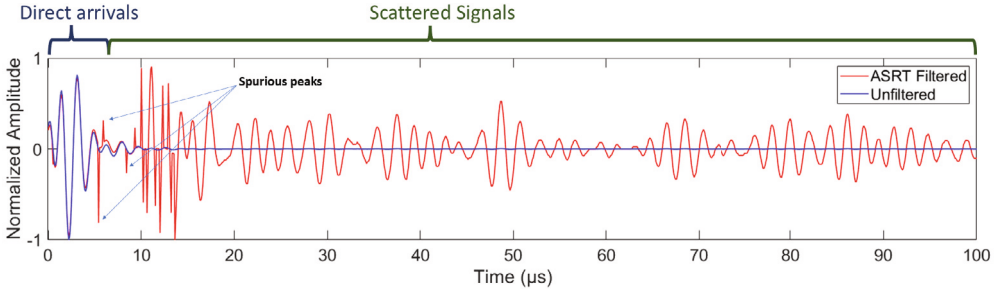


**Fig. 9.** Comparison between unfiltered (blue line) and ASRT-filtered (red line) received signals for the source 15-receiver 15 pair in the far-hole experimental case, normalized by their respective maximum values. The unfiltered case is dominated by the direct arrivals, which overshadow the rest of the signal. Using the ASRT-based technique, the scattered signals become visible. In this experimental case, the direct arrivals' relative amplitude is reduced to the same order of magnitude as the scattered signals, but they are not totally eliminated. Additionally, some spurious peaks are visible from Radon transform artifacts, but these are not found interfere significantly with TFM imaging. (For interpretation of the references to color in this figure legend, the reader is referred to the web version of this article.)

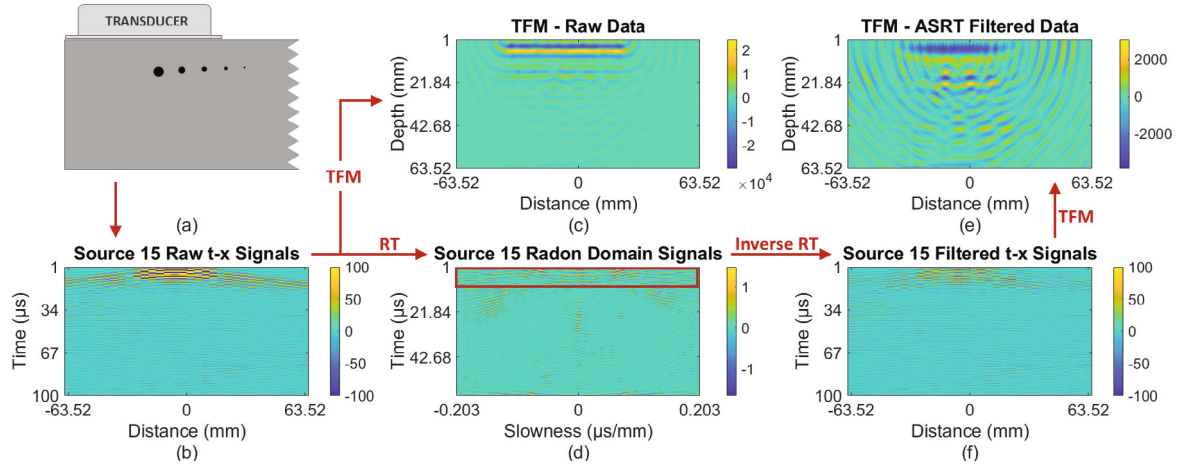


**Fig. 10.** The ASRT near-array artifact mute process is again applied to real data from an Inconel block with holes, this time with the block oriented with its holes near the transducer. In part (a), the Inconel specimen is represented in the close-hole orientation, from which the raw signals seen in part (b) are obtained. The poor results of raw TFM imaging is shown in part (c) where the holes in this case are unidentifiable. In part (d), the Radon transform is performed and the early-time curvature band of the Radon domain is muted at each source location. After filtering, TFM is performed to produce an image containing visible holes in part (e) from the filtered $t$ - $x$ signals in part (f).

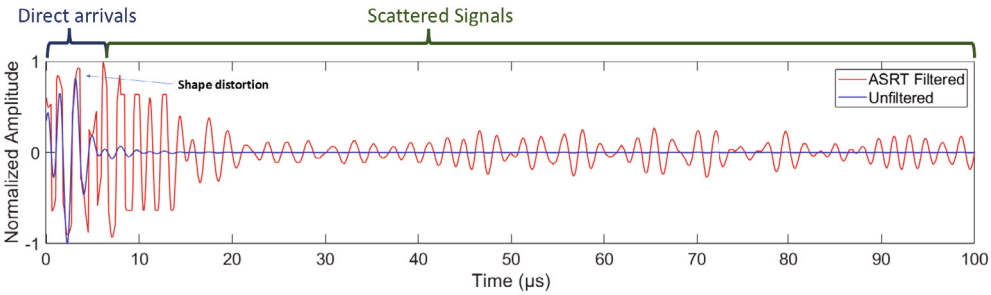


**Fig. 11.** Comparison of the unfiltered (blue line) and ASRT-filtered (red line) received signals for the source 15-receiver 15 pair, normalized by their respective maximum values for comparison. The unfiltered case is again dominated by the direct arrivals. The ASRT is used to mute the direct arrivals, making the response clearly visible. In this case, due to interactions between the scattered and direct arrival wave packets, the filtered signals have some shape distortion, but the frequency information is found to be preserved. (For interpretation of the references to color in this figure legend, the reader is referred to the web version of this article.)

**Table 2**
ASRT direct arrival mute power ratio $\frac{P_S}{P_R}$ comparison.

| Case | Unfiltered $\frac{P_S}{P_R}$ (dB) | Filtered $\frac{P_S}{P_R}$ (dB) | Improvement (dB) |
|---|---|---|---|
| Numerical steel domain | −45.008 | −6.285 | 38.723 |
| Experimental inconel block (Far) | −42.438 | −4.240 | 38.198 |
| Experimental inconel block (Close) | −41.791 | −12.575 | 29.217 |

## 5. Discussion

From the results presented here, the apex-shifted Radon transform is an effective tool for selectively filtering $t$ - $x$ domain data, and the results of this filtering process are shown to enhance ultrasonic imaging with TFM. In both cases, the ASRT filtering technique reduces the amplitude of the target wave packets by about 90% when combined with a thresholding task to limit the initial amplitude of the direct arrivals to just above the amplitude of the other received signals. The ASRT is easily paired with several simple filtering tasks, including thresholding, linear moveout correction (LMO), and simple attenuation correction, which can all situationally be employed to improve the final result.

From the results in the experimental data section, specifically in Fig. 8(f), it can be observed that the ASRT removes more of the direct arrivals from near the apex (at the source x-coordinate) than at the "tails", which can be seen in greater detail in Fig. 12. This is a known phenomenon due to the *spatial truncation effect*, which occurs when the theoretically infinite Radon domain is represented in a finite approximation [29]. Because of this approximation, energy pockets in the Radon domain are only mostly focused, and some of their energy is distributed throughout the rest of the Radon domain. When the filtering is performed, the high-density region is removed, but the uncollected portions remain, which are reconstructed in the observed "tails". Here, an LMO is useful since the ASRT is better at focusing on 0-slope linear shapes than sloped ones.

Aside from the truncated $q$-axis, another important characteristic of the Radon domain is the periodicity of the $\tau$ axis. If a wave packet intercepts the target apex outside the $t$ (time) boundaries of the $t$ - $x$ domain, it will be collected in the Radon domain at a $\tau$ location on the other end of the $\tau$ axis. For instance, if a linear wave packet would intercept the apex location $y$ 3 μs before the acquisition window begins, then it would exist in the Radon domain at $\tau = n_t - 3 \times 10^{-6}$, as seen in Fig. 13. This is sometimes important for filtering the entirety of a target wave group, which may "spill" into the opposite end of the $\tau$ axis of the Radon domain.

## 6. Conclusion

This paper has demonstrated the use of the apex-shifted Radon transform to enable near-array imaging in the total focusing method. From the results presented here, it is concluded that the ASRT is an effective tool for heavily attenuating the direct arrival wave groups in the $t$ - $x$ domain, and the presented methodology is shown to successfully increase the visibility of detected defects in TFM images for both numerical and experimental cases. The results presented in this work indicate a positive outlook for the ASRT as an ultrasonic nondestructive evaluation preprocessing technique.

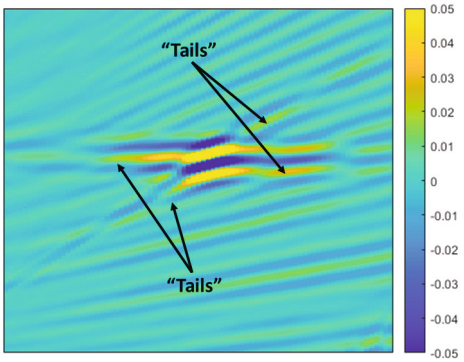


**Fig. 12.** A representative well-focused Radon domain representation of a wave packet including the dispersive "tails" containing information about the portion of the captured wave packet located far from the apex. A naive filtering procedure may not capture these tails, leading to an incomplete capture of the target wave packet.

First, the theory of the apex-shifted Radon transform is briefly outlined, and an intuitive working principle is described. Next, an illustrative numerical example is presented to clearly demonstrate how the ASRT can be used to mute the direct arrivals, heavily reducing the signature of the obscuring artifact. Then, an experimental case is presented where an Inconel block is scanned with a 0.5 MHz transducer, producing a large near-array artifact. The ASRT is again found to be effective in significantly reducing the signature of the artifact.

Several avenues exist to improve this technique. The high-resolution Radon transform is an iteratively optimized solution to the Radon transform that can be employed to better focus the Radon domain. With a higher-resolution Radon domain, the muting of target wave groups will be more effective.

In this paper, this technique has only been demonstrated on linear arrays. The $t$ - $x$ domain representation of wave groups received by different array geometries, such as ring arrays or 2-D arrays, will require different Radon domain formulations to successfully filter.

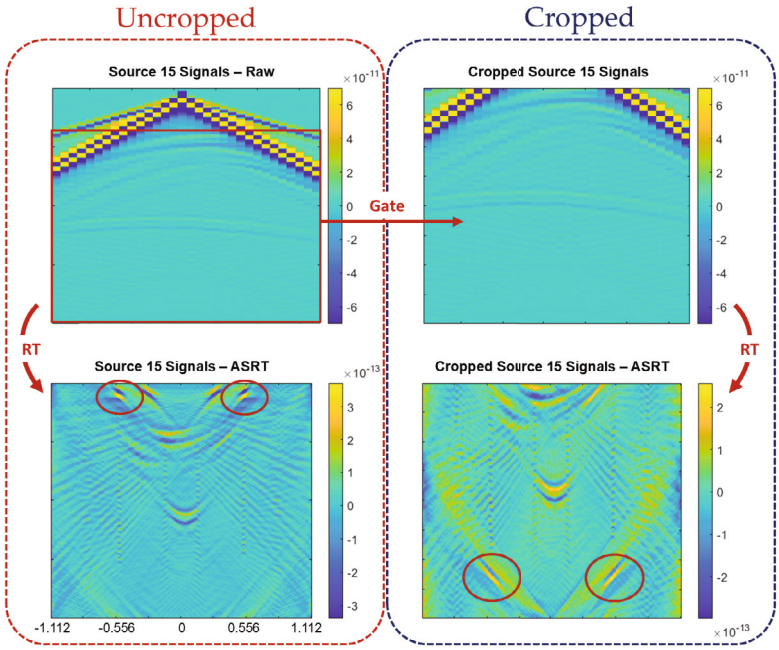


**Fig. 13.** The periodic nature of the time-axis of the Radon domain demonstrated by comparing the Radon transform of the numerically generated received signals for the steel, as in Fig. 4(b) and (d). The surface waves are collected in the Radon domain at the expected time coordinate of their intercept (left) at the top of the time-axis (highlighted by red circles). The signals are then time-gated or "cropped" for comparison (right), yielding a Radon domain where the surface wave signature is found at the bottom of the time-axis. The signature from the direct waves are not visible in this case, being located outside the cropped region.

## CRediT authorship contribution statement

**Augustine E. Loshelder:** Writing – review & editing, Writing – original draft, Investigation, Formal analysis, Data curation. **Jiaze He:** Writing – original draft, Supervision, Methodology, Funding acquisition, Conceptualization. **John D. Day:** Writing – review & editing, Validation. **Md. Aktharuzzaman:** Methodology. **Weihua Su:** Writing – review & editing, Supervision, Resources.

## Declaration of competing interest

The authors declare that they have no known competing financial interests or personal relationships that could have appeared to influence the work reported in this paper.

## Acknowledgment

This research was financially supported by the University of Alabama Graduate Council Fellowship, United States.

## Data availability

Data will be made available on request.

## References

[1] Del Rıo L, Jimenez A, Lopez F, Rosa F, Rufo M, Paniagua J. Characterization and hardening of concrete with ultrasonic testing. Ultrasonics 2004;42(1–9):527–30. http://dx.doi.org/10.1016/j.ultras.2004.01.053.

[2] Marais J, Mistry K. Rail integrity management by means of ultrasonic testing. Fatigue Fract Eng Mater Struct 2003;26(10):931–8. http://dx.doi.org/10.1046/j.1460-2695.2003.00668.x.

[3] Javadi Y, Pirzaman HS, Raeisi MH, Najafabadi MA. Ultrasonic inspection of a welded stainless steel pipe to evaluate residual stresses through thickness. Mater Des 2013;49:591–601. http://dx.doi.org/10.1016/j.matdes.2013.02.050.

[4] Garnier C, Pastor M-L, Eyma F, Lorrain B. The detection of aeronautical defects in situ on composite structures using non destructive testing. Compos Struct 2011;93(5):1328–36. http://dx.doi.org/10.1016/j.compstruct.2010.10.017.

[5] Nesvijski EG. Some aspects of ultrasonic testing of composites. Compos Struct 2000;48(1–3):151–5. http://dx.doi.org/10.1016/s0263-8223(99)00088-4.

[6] Honarvar F, Varvani-Farahani A. A review of ultrasonic testing applications in additive manufacturing: Defect evaluation, material characterization, and process control. Ultrasonics 2020;108:106227. http://dx.doi.org/10.1016/j.ultras.2020.106227.

[7] Rieder H, Dillhöfer A, Spies M, Bamberg J, Hess T. Online monitoring of additive manufacturing processes using ultrasound. In: Proceedings of the 11th European conference on non-destructive testing. Vol. 1, 2014, p. 2194–201. http://dx.doi.org/10.31399/asm.hb.v24A.a0006968.

[8] Silk M. Defect detection and sizing in metals using ultrasound. Int Met Rev 1982;27(1):28–50. http://dx.doi.org/10.1179/imr.1982.27.1.28.

[9] Schafer ME. Ultrasound for defect detection and grading in wood and lumber. In: 2000 IEEE ultrasonics symposium. proceedings. an international symposium (cat. no. 00CH37121). Vol. 1, IEEE; 2000, p. 771–8. http://dx.doi.org/10.1109/ultsym.2000.922658.

[10] Chaix J-F, Garnier V, Corneloup G. Ultrasonic wave propagation in heterogeneous solid media: Theoretical analysis and experimental validation. Ultrasonics 2006;44(2):200–10. http://dx.doi.org/10.1016/j.ultras.2005.11.002.

[11] Loveday P, Ramatlo D, Burger F. Monitoring of rail track using guided wave ultrasound. In: Proceedings of the 19th world conference on non destructive testing. 2016, p. 3341–8. http://dx.doi.org/10.1063/1.5031566.

[12] Yu X, Zuo P, Xiao J, Fan Z. Detection of damage in welded joints using high order feature guided ultrasonic waves. Mech Syst Signal Process 2019;126:176–92. http://dx.doi.org/10.1016/j.ymssp.2019.02.026.

[13] Katunin A, Dragan K, Dziendzikowski M. Damage identification in aircraft composite structures: A case study using various non-destructive testing techniques. Compos Struct 2015;127:1–9. http://dx.doi.org/10.1016/j.compstruct.2015.02.080.

[14] Ogi H, Hayama N, Niho H, Hirao M, Morishita T. Imaging of local stiffness of damaged polycrystalline copper: Nondestructive evaluation by resonance ultrasound microscopy. IEEE Trans Ultrason Ferroelectr Freq Control 2007;54(8):1514–20. http://dx.doi.org/10.1109/tuffc.2007.421.

[15] Holmes C, Drinkwater B, Wilcox P. The post-processing of ultrasonic array data using the total focusing method. Insight, Non-Destr Test Cond Monit 2004;46(11):677–80. http://dx.doi.org/10.1784/insi.46.11.677.52285.

[16] Zhang J, Drinkwater BW, Wilcox PD, Hunter AJ. Defect detection using ultrasonic arrays: The multi-mode total focusing method. NDT E Int 2010;43(2):123–33. http://dx.doi.org/10.1016/j.ndteint.2009.10.001.

[17] Camacho J, Parrilla M, Fritsch C. Phase coherence imaging. IEEE Trans Ultrason Ferroelectr Freq Control 2009;56(5):958–74. http://dx.doi.org/10.1109/TUFFC.2009.1128.

[18] He J, Rao J, Fleming JD, Gharti HN, Nguyen LT, Morrison G. Numerical ultrasonic full waveform inversion (FWI) for complex structures in coupled 2D

solid/fluid media. Smart Mater Struct 2021;30(8):085044. http://dx.doi.org/10.1088/1361-665x/ac0f44.
[19] McClung R. The immersed ultrasonic inspection of metal plate, Research Report. (ORNL-2650). Oak Ridge, Tennessee: Oak Ridge National Laboratory; 1959.
[20] Hanafy A. Dead zone elimination in acoustic arrays. Ultrason Imaging 1980;2(4):302–12. http://dx.doi.org/10.1177/016173468000200402.
[21] Jin S-j, Wang Z-c, Yang Y-n, Luo Z-b. Corrected mode-converted wave method for detecting defects in tofd dead zone. J Nondestruct Eval 2023;42(3):62. http://dx.doi.org/10.1007/s10921-023-00975-5.
[22] Fan C, Yang L, Zhao Y. The pre-processing of ultrasonic array data for time-reversal-based imaging algorithm. In: 2017 far east NDT new technology & application forum. FENDT, IEEE; 2017, p. 13–7. http://dx.doi.org/10.1109/fendt.2017.8584591.
[23] Lin X, Yuan F. Detection of multiple damages by prestack reverse-time migration. AIAA J 2001;39(11):2206–15. http://dx.doi.org/10.2514/2.1220.
[24] Ha JM, Seung HM, Choi W. Autoencoder-based detection of near-surface defects in ultrasonic testing. Ultrasonics 2022;119:106637. http://dx.doi.org/10.1016/j.ultras.2021.106637.
[25] Trad D, Siliqi R, Poole G, Boelle J-L. Fast and robust deblending using apex shifted radon transform. In: SEG technical program expanded abstracts 2012. Society of Exploration Geophysicists; 2012, p. 1–5. http://dx.doi.org/10.1190/segam2012-0703.1.
[26] Hargreaves N, verWest B, Wombell R, Trad D. Multiple attenuation using an apex-shifted radon transform. In: SEG international exposition and annual meeting. SEG; 2003, p. SEG–2003. http://dx.doi.org/10.1190/1.1817699.
[27] Radon J. On the determination of functions from their integral values along certain manifolds. IEEE Trans Med Imaging 1986;5(4):170–6. http://dx.doi.org/10.1109/TMI.1986.4307775.
[28] Zhang Q, Wang H, Chen W, Huang G. A local radon transform for seismic random noise attenuation. J Appl Geophys 2021;186:104264. http://dx.doi.org/10.1016/j.jappgeo.2021.104264.
[29] Wang Y. Multiple attenuation: Coping with the spatial truncation effect in the radon transform domain. Geophys Prospect 2003;51(1):75–87. http://dx.doi.org/10.1046/j.1365-2478.2003.00355.x.
[30] Loshelder AE, He J, Aktharuzzaman M, Harb MS, Rao J. Apex-shifted radon transform for baseline-subtraction-free (BSF) damage scattered wave extraction. Struct Heal Monit 2023;14759217231156364. http://dx.doi.org/10.1177/14759217231156364.
[31] Drinkwater BW, Wilcox PD. Ultrasonic arrays for non-destructive evaluation: A review. NDT E Int 2006;39(7):525–41. http://dx.doi.org/10.1016/j.ndteint.2006.03.006.
[32] Long R, Russell J, Cawley P. Ultrasonic phased array inspection using full matrix capture. Insight, Non-Destr Test Cond Monit 2012;54(7):380–5. http://dx.doi.org/10.1784/insi.2012.54.7.380.
[33] Tromp J, Komatitsch D, Liu Q. Spectral-element and adjoint methods in seismology. Commun Comput Phys 2008;3(1):1–32.
[34] Kumar V, Silwal V, Ray S. Simulation of seismic wave propagation using spectral-element method for Uttarakhand Himalayan Region with Specfem3D. In: 2nd EAGE/aqua foundation Indian near surface geophysics conference & exhibition. Vol. 2023, European Association of Geoscientists & Engineers; 2023, p. 1–5. http://dx.doi.org/10.3997/2214-4609.202375052.
[35] Chow B, Kaneko Y, Tape C, Modrak R, Townend J. An automated workflow for adjoint tomography—Waveform misfits and synthetic inversions for the North Island, New Zealand. Geophys J Int 2020;223(3):1461–80. http://dx.doi.org/10.1093/gji/ggaa381.
[36] Modrak RT, Borisov D, Lefebvre M, Tromp J. Seisflows—Flexible waveform inversion software. Comput Geosci 2018;115:88–95. http://dx.doi.org/10.1016/j.cageo.2018.02.004.